CHARACTERIZATIONS OF ANNEALED ION IMPLANTED SILICON CARBIDE MATERIALS AND DEVICES

by

Xin Zhang

A thesis submitted to the Faculty of the University of Delaware in partial fulfillment of the requirements for the degree of Master of Electrical Engineering.

Fall 2005

UMI Number: 1430756

UMI Microform 1430756

ProQuest Information and Learning Company
300 North Zeeb Road
P.O. Box 1346
Ann Arbor, MI 48106-1346

CHARACTERIZATIONS OF ANNEALED ION IMPLANTED SILICON CARBIDE MATERIALS AND DEVICES

by

Xin Zhang

Approved: _____
James Kolodzey, Ph.D.
Professor, Department of Electrical and Computer Engineering

Approved: _____
Gonzalo R. Arce, Ph.D.
Chair of the Department of Electrical and Computer Engineering

Approved: _____
Eric W. Kaler, Ph.D.
Dean of the College of Engineering

Approved: _____
Conrado M. Gempesaw II, Ph.D.
Vice Provost for Academic and International Programs

ACKNOWLEDGMENTS

I am indebted to a number of people who helped make this work possible, and for their assistance and support throughout my graduate research at the University of Delaware. I gratefully acknowledge Dr. James Kolodzey, my adviser, for guidance, support, encouragement and assistance with my research. I would like to thank many colleagues Dr. Thomas Adam, Dr. Mike Dashiell, Dr. Pengcheng Lv, Dr. Kristopher Roe, and Dr. Thomas Troeger for many fruitful discussions. I am indebted to Dr. Keith Goossen, and Dr. Ian Appelbaum for generous sharing of lab facilities.

I would also like to thank many students that I had the pleasure to work with: Matthew Coppinger, Suddhasatwa Ghosh, Sangcheol Kim, Ulrike Lehmann, Paola Murcia, Nathan Sustersic, Guangchi Xuan.

During this research, I had the pleasure of co-operating with many people outside the University of Delaware. I would like to acknowledge Dr. Greg Desalvo (Northrop Grumman), and Dr. Adrian Powell (Cree Inc.)

Last, but not the least, I want to thank Charles Hanavin, Williams Rule, and Larry Smith for their technical helps in assembling the high temperature annealing furnace.

This work was supported by CRDF Award No. RP2-2552-MO-02, ONR grant No. N00014-03-1-0758 and AFOSR under contract number N0001-4-00-1-0834.

TABLE OF CONTENTS

LIST OF TABLES

LIST OF FIGURES

ABSTRACT

Silicon carbide (SiC) materials have unique materials properties, such as high good thermal conductivity ,high saturated velocity and high breakdown field, which make them attractive many applications in the areas of high temperature, high frequency and high power devices. Despite of the superior materials properties of SiC as listed above , it is difficult to fabricate SiC devices with conventional silicon CMOS technology. One of the difficulties is to introduce dopants into SiC. Unlike silicon, the introduction of dopants into SiC was mainly done with ion implantation. The lattice damage and strain caused by ion implantation needs to be removed by high temperature annealing. Therefore, a major part of this thesis was to design and realize a high temperature annealing furnace to remove the lattice damage and strain. Annealed samples were analyzed with high resolution X-Ray diffraction and Fourier Transform Infrared Spectroscopy. Our results suggest that high temperature thermal annealing can remove the strain and damage caused by ion implantation.

Recent advances in impurity doped silicon terahertz emitters motivated us to study the possibility of using nitrogen doped 4H-SiC devices as terahertz emitters. Due to the two non- equivalent donor sites of nitrogen in 4H- SiC, for the first time, strong terahertz emission was observed up to temperatures of 150K. This result suggest that it

may be possible to use SiC terahertz emitters for high temperature, high power portable applications.

Chapter 1

INTRODUCTION AND MOTIVATION

Silicon is the material dominating the electronics industry today. Compared to silicon, Silicon carbide (SiC) materials, however, have superior properties, such as good thermal conductivity ,high breakdown electric field and high saturated velocity, which are suitable for high temperature, high frequency and high power device applications.[1,2] A change of technology from silicon to silicon carbide will revolutionize the semiconductor industry. For instance, it will be economically feasible to use power electronics to a much larger extent than today to control engines. Not only that, recent discoveries about new applications of SiC materials for many novel applications, such as SiC: Ge heterojunction bipolar transistor (HBT), [3-6] terahertz emitters and light emitting devices make SiC research meaningful. In the following section, I will briefly introduce the SiC materials and their properties, which will be compared with other commercial semiconductor materials such as Si and GaAs.

1.1 Introduction to Silicon Carbide materials

Silicon Carbide possesses many favorable properties making it interesting for high-temperature, high-frequency and high-power and high radiation applications. More specifically, these properties are: wide bandgap, high thermal conductivity (for example better than copper at room temperature), high breakdown electric field

strength (approximately 10 times that of Si), [7] high saturated drift velocity (higher than GaAs), high thermal stability ,and chemical inertness.

Owing to the differing arrangement of silicon and carbon atoms within the SiC crystal lattice, each SiC polytype exhibits unique electrical and optical properties.[8] Some of the more important semiconductor electrical properties of the 3C, 4H, and 6H silicon carbide polytypes at room temperature are given in Table1.1. [9] For comparison, Table 1.1 also includes comparable properties of Silicon and GaAs. Because silicon is the semiconductor employed in most commercial solid-state electronics, it is the yardstick by which other semiconductor materials must be evaluated against.

Table 1.1: Comparison of properties of selected SiC polytypes with silicon and GaAs(T=300K). [9]

Property	Si	GaAs	4H-SiC	6H-SiC	3C-SiC
Bandgap (eV)	1.12	1.42	3.2	3.0	2.3
Relative dielectric constant	11.9	13.1	9.7	9.7	9.7
Breakdown field at $N_D = 10^{17} cm^{-3}$ ($MVcm^{-1}$)	0.6	0.6	∥c-axis 3.0	∥c-axis 3.2 ⊥c-axis >1	> 1.5
Thermal conductivity ($Wcm^{-1}K^{-1}$)	1.5	0.5	3-5	3-5	3-5
Intrinsic carrier concentration(cm^{-3})	10^{10}	$1.8x10^6$	$\sim 10^{-7}$	$\sim 10^{-5}$	~10
Electron mobility at $ND=10^{16} cm^{-3}$ ($cm^2V^{-1}S^{-1}$)	1200	6500	∥c-axis 800 ⊥c-axis 800	∥c-axis 60, ⊥c-axis 400	750
Hole mobility at $NA=10^{16} cm^{-3}$ ($cm^2V^{-1}s^{-1}$)	420	320	115	90	40
Saturated electron velocity($10^7 cms^{-1}$)	1.0	1.2	2	2	2.5

1.2 Motivation for this work

Despite of the superior properties of SiC, the conventional silicon process can not be directly applied to SiC device fabrication. Many problems are still remained to fabricate SiC devices. For example, Ohmic contacts can easily be formed with various metals on silicon, however, it is tricky to form Ohmic contacts with SiC materials. Moreover, oxidation of si can be used to form the conventional gate dielectric materials SiO_2, but it is very difficult to form oxide with simple oxidation process on SiC. Chemical vapor deposition (CVD) has to be used to deposite gate dielectrics on SiC. Because of its extreme stability, the introduction of dopants into SiC can't be done with thermal diffusion, as is commonly done in silicon processing. Instead, dopants are introduced by ion implantation.

Once implanted into the crystal, the dopant atoms occupy interstitial positions in the lattice and must be transferred to substitutional sites to become electrically active. This "activation" is accomplished by high temperature annealing in an inert ambient such as argon. A standard process to introduce dopants into SiC with ion implantation and annealing is described as follows: [10] Implantation is usually conducted with the sample at an elevated temperature (600 - 800 ^{o}C) to provide some in-situ annealing of lattice damage caused by the implant. The implanted sample is subsequently annealed at temperatures between 1000 - 1700 ^{o}C for times between 5

and 90 minutes to activate the dopants. The dynamics of activation depends both on the dopant species (i.e. aluminum vs boron, nitrogen vs phosphorus) and upon the SiC polytype (i.e. 4H vs 6H). Because ion implantation can also cause strains and defects in the crystal, which will dramatically reduce the carrier lifetime, and should be avoided for applications such as emitters and HBTs, high temperature annealing is a must to relax the strains. Therefore, it is very useful and meaningful to assemble a high temperature annealing furnace.

One major part of this thesis is to design and assemble a high temperature annealing furnace to anneal implanted SiC materials.

1.3 Outline of the thesis

Chapter 2 will outline the setup and components of a high temperature annealing furnace. In chapter 3, properties of the annealed Ge implanted SiC materials were analyzed by high resolution X- Ray diffraction, high resolution Transmission Electron Microscopy (HRTEM), and Fourier Transform Infrared Spectroscopy (FTIR). A novel application of nitrogen doped 4H- SiC devices as terahertz emitters will be discussed in Chpater 4. Chapter 5 summarizes the work.

Chapter 2

EXPERIMENTAL SETUP OF HIGH TEMPERATURE ANNEALING FURNACE

In this chapter, the parts and the final setup of the annealing furnace are described. I will first outline the parts and their specifications, and then describe the assembled furnace. The operation and heater replacement procedures for the furnace will also be included.

2.1 The parts of the annealing furnace

The major parts of the annealing furnace are listed below:

- Split tube furnace
- Al_2O_3 tube
- Control system
- Over temperature control system
- Cooling system
- Vacuum pump, vacuum meters and gas flow meters

The split tube furnace shown in Fig. 2.1 has a heating chamber cavity dimension of 5 inch inner diameter and 10 inch long. The overall external dimensions are 22 inch high, 22 inch wide and 24 inch deep. It uses 40V single phase power, and the maximum operating temperature is 1700 ^{o}C. The heating elements are made of molybdenum disilicide, and the heating power is 5.5 kW. To ensure the uniform temperature distribution in the heating zone, three heating elements on both sides of the tube are used, and in series connection with each other, as shown in Fig. 2.2. Light weight ceramic fiber was used as insulation, and the shell is welded heavy gauge stainless steel.

Since the annealing temperature of SiC is very high (1200^{0}C~1650^{0}C), we selected Al_2O_3 as tube material. The ceramic tube has 4.8 inch inner diameter, 5 inch external diameter and a 4- foot length. The control system needs 230V, 1phase, 60 cycle electrical power. The voltage in our lab is 208V, and is lower than the required voltage. To satisfy the voltage and power requirements of the furnace, a buck-boost transformer (manufacturer: square D, and catalog number 1S43F) was used to increase the incoming voltage to 230V. The buck & boost transformer is an isolating transformer that has a 120Vx 240V primary and a 12/24V secondary. The primary and secondary of the buck & boost transformer can be interconnected for use as an autotransformer to slightly step up or down voltage. The wiring diagram of the transformer is shown in Fig. 2.3. When used as an autotransformer to slightly adjust

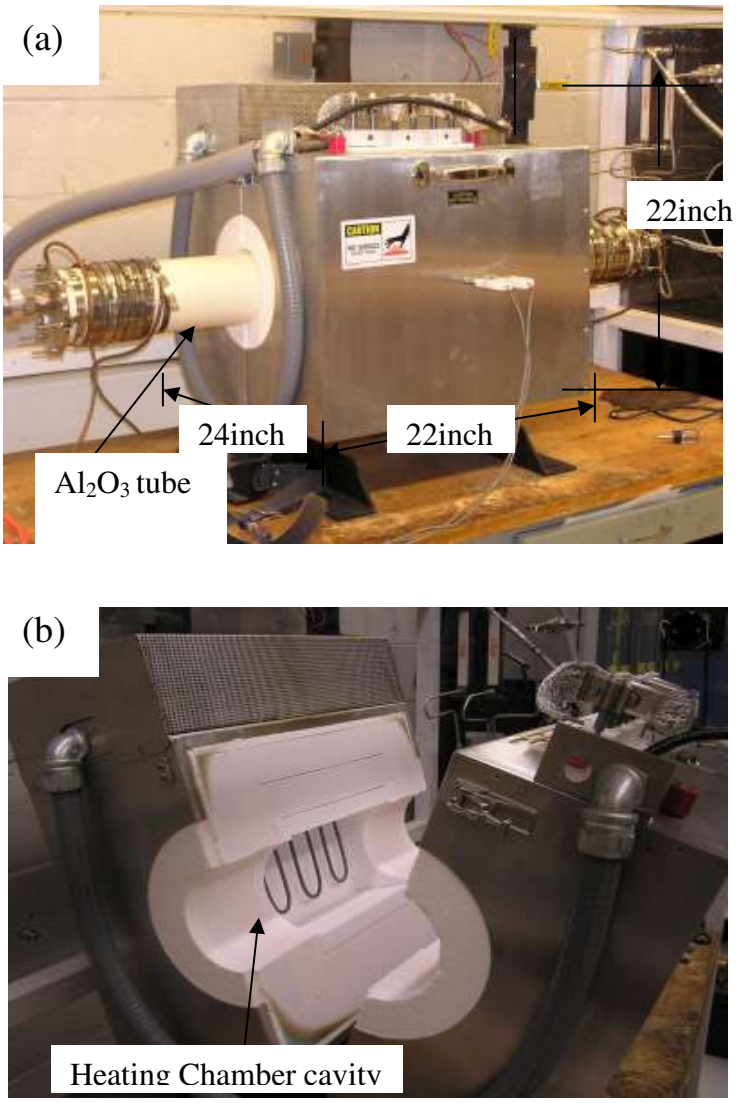

Figure 2.1: **(a) A picture of the split tube furnace. The dimension of the split tube furnace is 22inch high,22inch wide and 24inch deep, (b) A picture of the inner heating cavity (5inch inner diameter and 10 inch long), the heating elements are also shown.**

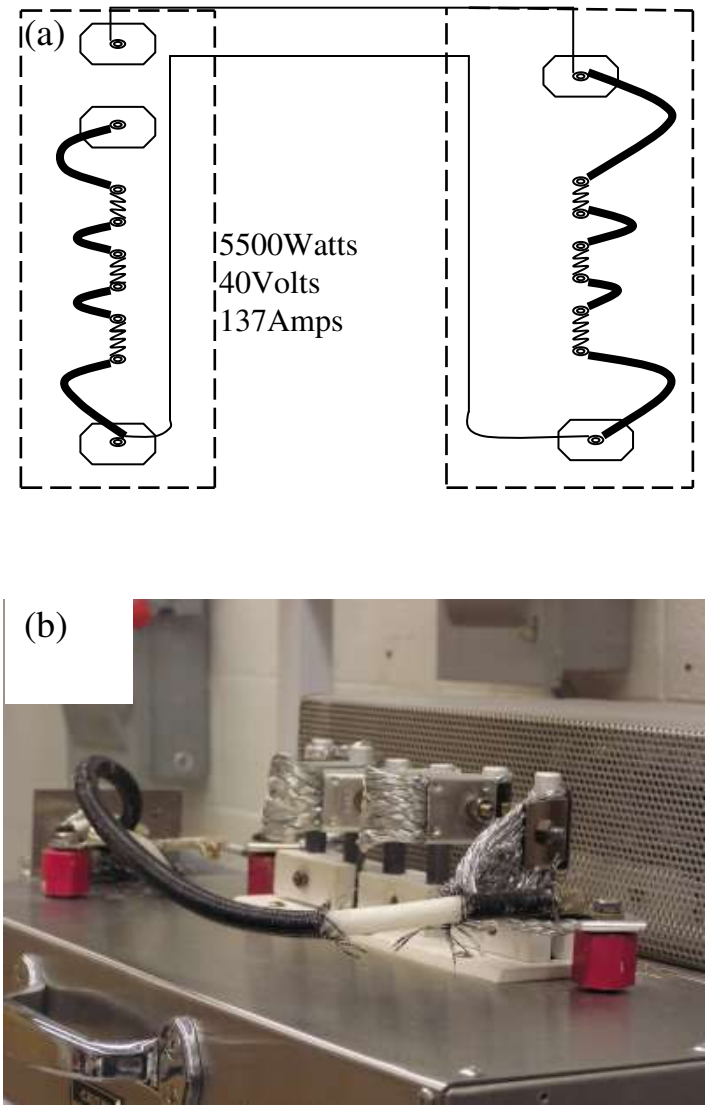

Figure 2.2: **(a) A schematic of the heating elements of the split tube furnace. The materials for the heating elements are molybdenum disilicide, and they are in series connection with each other, (b) A picture of the heating elements.**

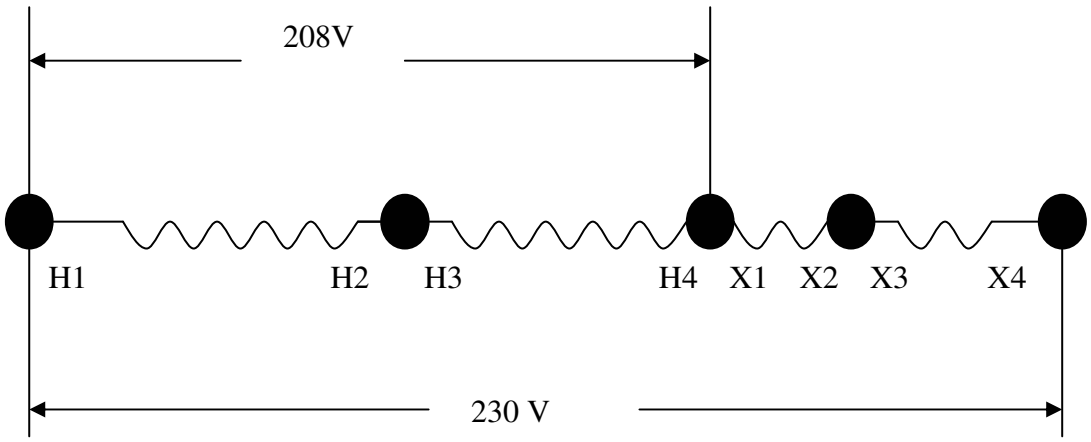

Figure 2.3: Wiring diagram of the Buck & Boost transformer to transform the 208V to 230 V as required by the control system. The single phase load in this wiring setting is 9 kW, which is greater than the maximum heating power requirement (5.5 kW).

voltage, the buck & boost transformer can carry loads in excess of its nameplate rating. With various wiring options of the transformer, the input voltage (208V) can be transformed to 189, 198, 218, and 229V. Correspondingly, the single phase load at these voltages are 8.6, 17.3, 18.1, and 9.5 kW. Therefore, we used the Buck & Boost transformer solved the voltage requirements. The control system includes another transformer which can transform input voltage from 230V to 40 V, and a PID controller which can control the amount of power to the resistive heating element in order to achieve and maintain the desired temperature as measured through the control thermocouple. The output current of the transformer is 24 Amps, and the temperature control system consists of set point temperature controller, solid state power controller, mechanical contactor and matching control thermocouple as shown in Fig 2.4.

If the temperature control system malfunctions and the temperature continues to rise above the setting point, the over temperature controller will shut the power off when the setting temperature is reached. The over temperature controller is usually set $50\ ^{0}F$ higher than the furnace chamber controller. Under no circumstances should the high limit set point be set higher than the maximum temperature of the furnace. Type B thermocouple (+ lead: platinum- 30% Rhodium, - lead: platinum- 6% Rhodium), which can sense a maximum temperature of 1700 ^{o}C with an error of 0.5% over $800^{o}C$, are used for both primary temperature control and over temperature control system. These two systems are set in a free standing steel cabinet, as shown in Fig. 2.5.

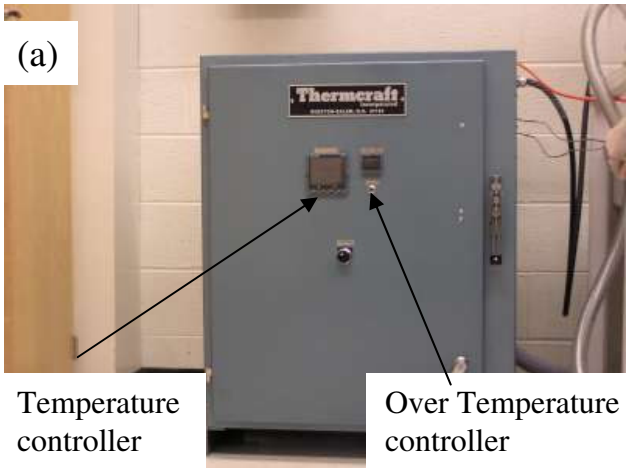

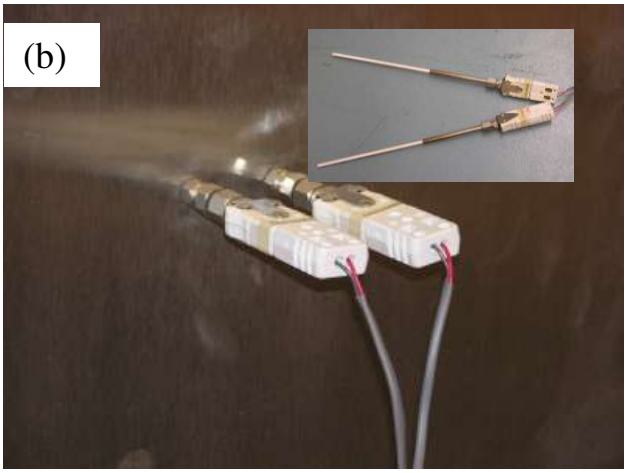

Figure 2.4: **(a) A picture of the temperature controller and over- temperature controller, showing two PID controllers. The temperature controller control the heating element, and the over- temperature controller prevents the heating elements being overheating. (b) Two type B thermocouples were used and mounted on the center zone of the split tube furnace, one for the temperature controller, the other for the over- temperature controller.**

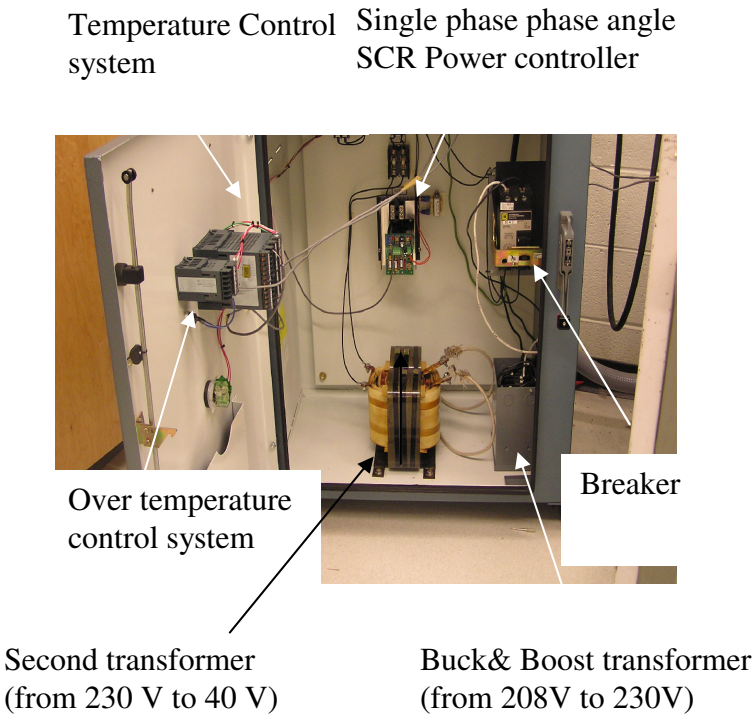

Figure 2.5: A picture showing the inner circuit structure of the temperature controller and the over temperature controller system. Two transformers were used to convert the 208V to 40V as required by the heating elements.

Since most of the annealing processes require vacuum. We used stainless steel endcaps with Viton O-rings to keep vacuum. Due to the constraint of the budget, we only bought a 4 feet long ceramic tube. This has caused a problem since the endcaps were so close (~1 feet) to the center heating zone. Therefore, the endcaps are very hot with a high heating zone temperature. The maximum temperature that the Viton O-rings can stand, however, is 150 ^{o}C. We first measured the temperatures at the endcaps without the Viton O- rings, and found that it was 275 ^{o}C at a center zone temperature of 1300 ^{o}C. In order to prevent the overheating of the O- rings at the endcaps, we fixed ¼" copper tub coils with clamps to the wall of the ceramic tube, and ran tape water through the tubing. Fig. 2.6 shows the temperature of the endcaps with and without the water cooling. As shown in Fig. 2.6, a dramatic reduction of the endcap temperature was achieved with water cooling. For example, the endcap temperature was 120 ^{0}C with water cooling as compared to 275 ^{o}C without water cooling at a center zone temperature of 1300 ^{o}C. Therefore, we solved the problem of the high temperatures on the endcaps with water cooling.

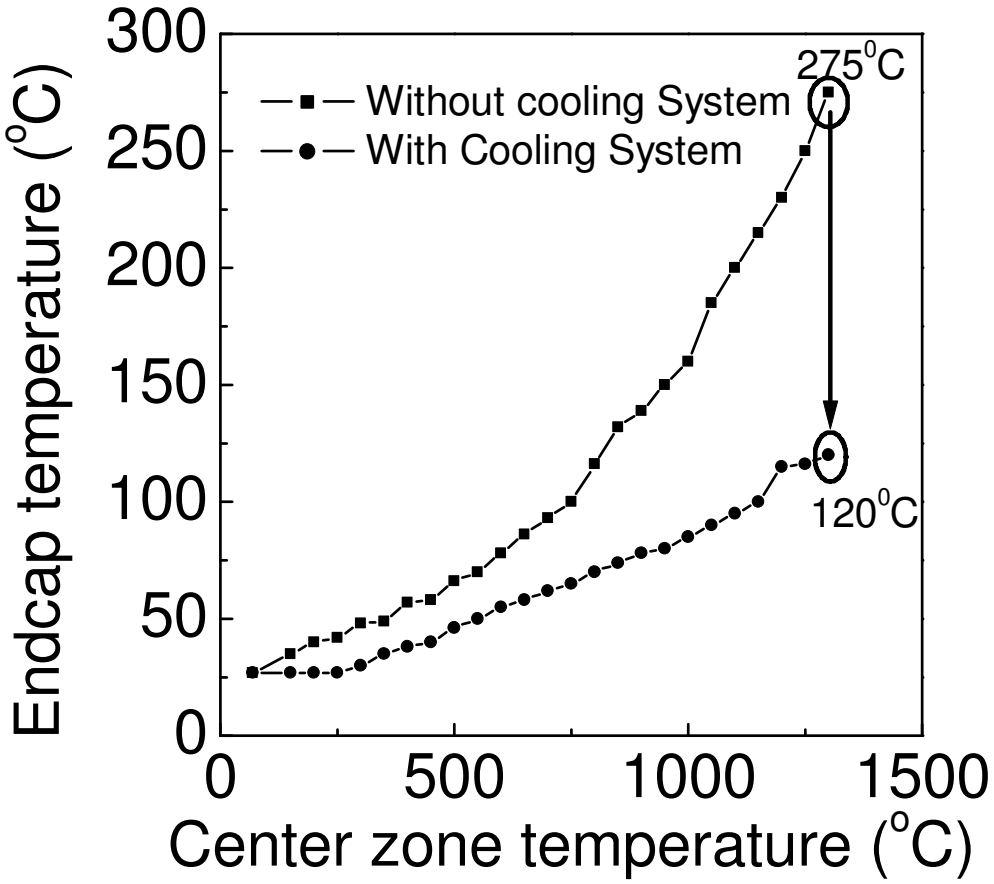

Figure 2.6: **The temperatures at the endcaps at various center zone temperatures, indicating that the endcap temperature increases faster at higher center zone temperatures.**

To evacuate the furnace tube, we used a mechanical pump, which can pump the system to 20 mTorr. The vacuum was measured with a thermocouple gauge. We also installed two gas flow meters and the necessary tubing to selectively use annealing gases, such as argon, nitrogen, and forming gas.

2.2 The assembled furnace

The whole assembled furnace is shown in Fig. 2.7 with each component marked. We tested the furnace, and found that the maximum operating temperature was 1450 ^{o}C, which was lower than the designed value, presumably because of the heat loss of the system. Basically, two major aspects caused the heat loss. One was due to the air gap between the heating chamber and the ceramic tube, and the other was due to the cooling at the endcaps, which compensated a portion of the heating power. Future improvement of the furnace including the use of insulation materials to fill in the air gap, and a longer ceramic tube so that cooling at the endcaps are not necessary.

The temperature of the center heating zone vs. time is shown in Fig. 2.8. Experimentally, the temperature was set to 50 ^{o}C, once the furnace reached the setting temperature, a new setting will be set on the PID controller with a step increase of 50 ^{o}C. For the first 800 ^{o}C, it took around 4 to 5 minutes for each step, but at the temperature higher than 800 ^{o}C, it took longer to the reach the setting temperature. The higher the setting temperature is, the longer it took for each step. These results suggest that the heat loss increased with increasing center zone temperature,

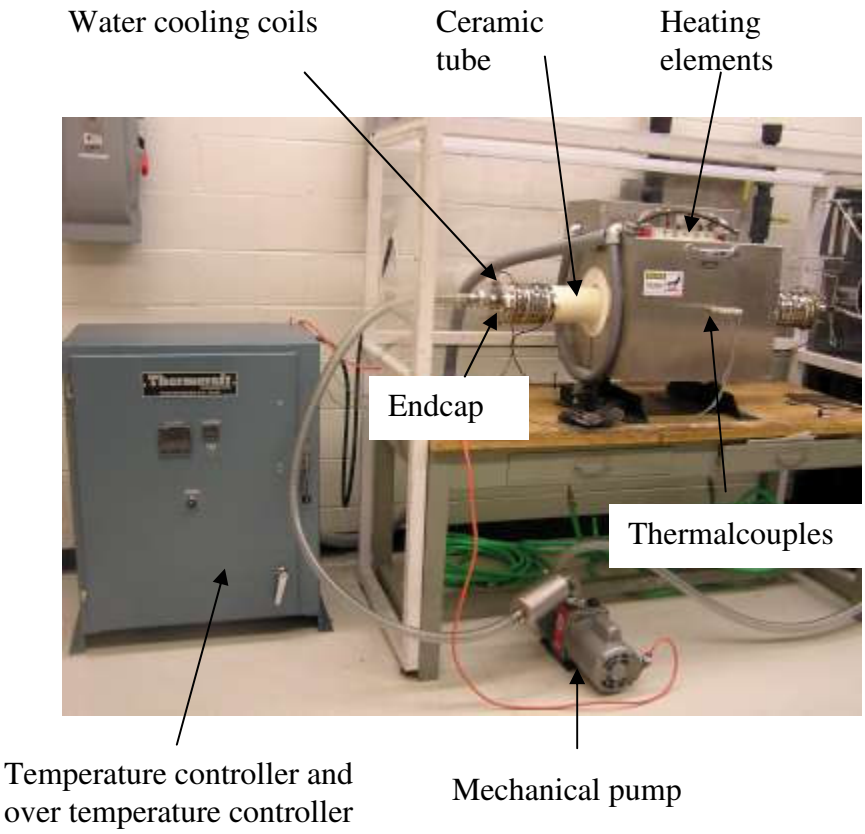

Figure 2.7: A picture of the assembled high temperature annealing furnace. The major parts are shown in the figure.

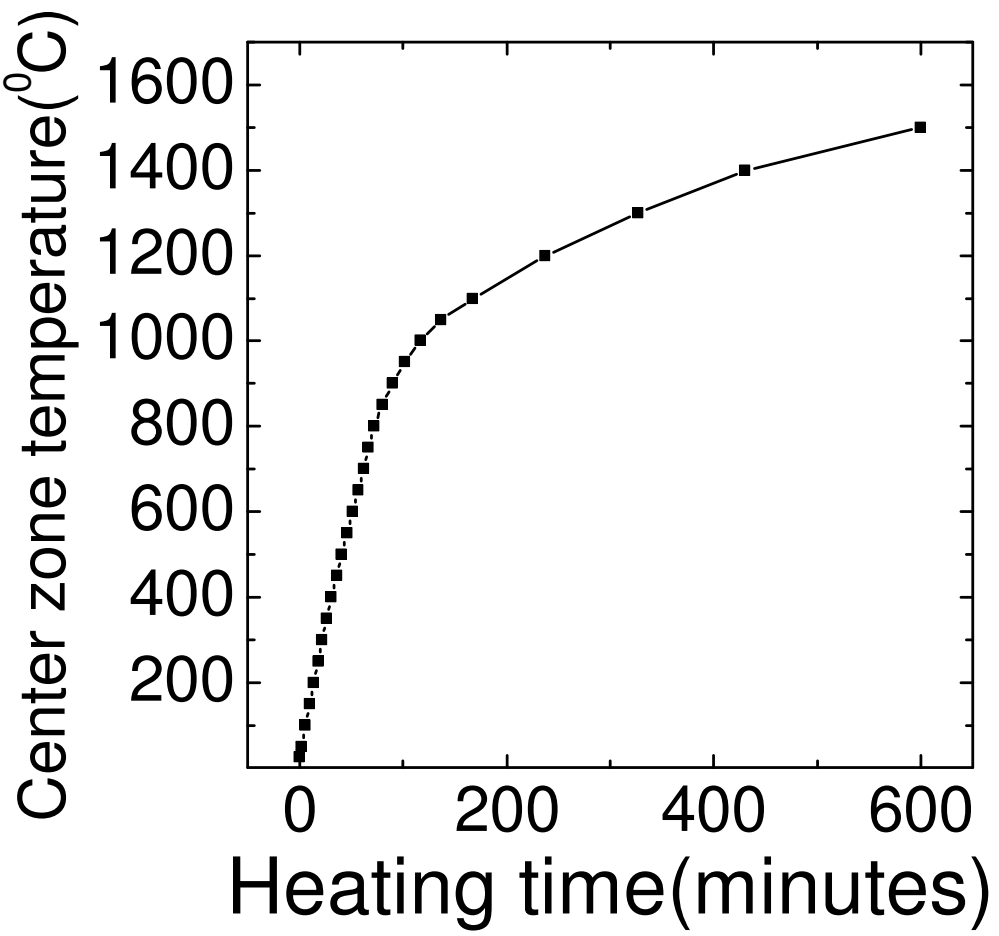

Figure 2.8: **The center zone temperature vs. cumulative heating time. The maximum temperature achievable with current setup was 1450 °C, it took longer to reach the setting temperature step at higher temperature.**

the temperature will reach an equlibrium once the heating rate equals to the heat loss rate.

2.3 Operational procedures and cautions

1. **Drying Out**. Before the initial heat up, Crack open the furnace door and remove the terminal box covers. Heat furnace slowly up to 200^0 F, this will dry the moisture out of the refractory lining. Keep furnace at 200^0 F for four to six hours. Be sure to turn off power prior to reattaching terminal box covers to prevent accidental shortage and potential for electrical shock. After reattaching the terminal box covers and closing the door, continue furnace heat up to normal operating temperature. If steaming appears at any time during run up, do not increase temperature until steaming stops.

2. **Sample loading**. Put the sample in a graphite boat as shown in Fig. 2.9, slowly transfer the sample with a quartz pushing rod to the center zone, which is 2 feet away from the end of the tube. Put on the Viton O-ring, and fix the endcaps to the tube with the 6 screws. Connect the mechanical pump, and start pumping.

3. **Furnace heating up**. Before the furnace heating up, turn on the tap cooling water to avoid overheating of the O-rings at the endcaps. Then set up the furnace temperature to 300 ^{o}C, once the temperature reach the setting temperature,

give a new setting with a step of 300 ^{o}C, until the furnace reached the desired annealing temperature.

4. **Annealing**. Anneal the sample with desired time duration.

5. **Shut down the furnace.** Open main circuit breaker or disconnect switch . The cooling water should be kept flowing through the copper tube until the furnace completely cools down.

To avoid the burnout of the heating element, cautions need to be taken. Specifically, do not allow any build up of foreign material on the element. Set up a schedule for as often as needed to either vacuum the elements or blow out the elements with compressed air. Oil should be cleaned off of parts prior to heating. Be careful not to move the element, as the element wire may be brittle and break.

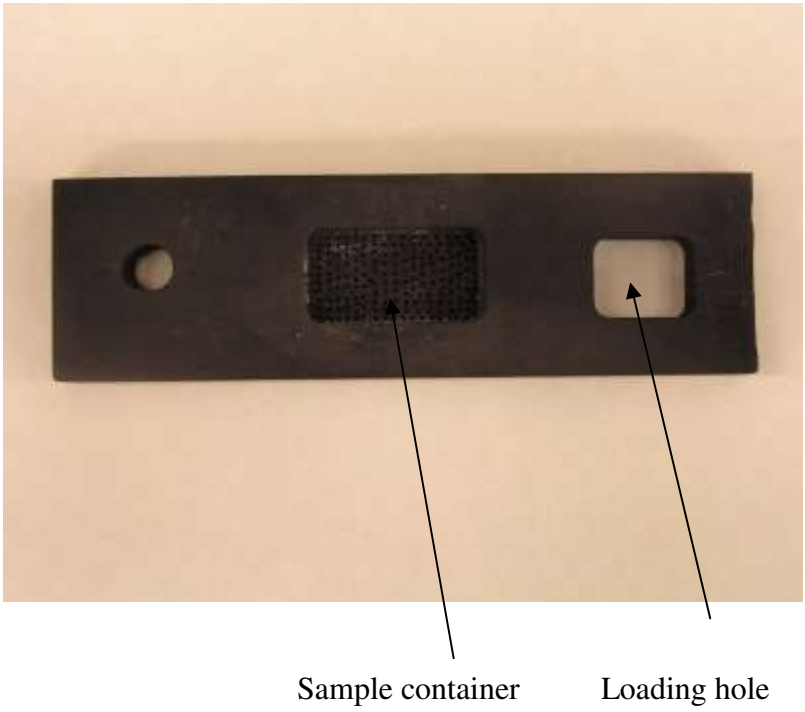

Figure 2. 9: A picture of the graphite sample boat. The annealing samples are loaded in the central sample container (~1/2 inch × 1 inch). The sample boat was loaded to the center heating zone with a quartz pushing rod via the loading hole.

2.4 Ceramic plate heater replacement procedures

1. Open furnace door, use “c” clamp as a safety precaution to hold door open.

2. Remove the terminal box cover, and loosen brass nuts holding leads of heater to be removed.

3. Straighten leads so that they will slide through the holes in the insulation.

4. Remove the hearth tray.

5. After removing the nuts and ceramic, remove any insulation surrounding the heater, and remove hanger bolts holding the heat in place.

6. Remove any ceramic beads or tubes on the old heater leads and put them on the new heater leads.

7. Insert leads of new heater into holes in the insulation, and position the heater(do not force)

8. Replace hanger bolts and tighten. Be careful not to tighten too much, heater damage may occur.

9. Replace insulation and hearth plate, and wrap heater leads clockwise around brass studs and tighten(do not overlap leads).

10. Cut off excess lead materials, such as wires, and tighten brass nuts holding leads of heater.

Chapter 3

CHARACTERIZATION OF ANNEALED GERMANIUM IMPLANTED SILICON CARBIDE FILMS

In this chapter, four sets of nitrogen doped 4H-SiC samples (ρ = 0.059 Ohm.cm) with different doses were implanted with Ge^+ ions. [11] The implantation temperature was 1000 ^{0}C, and the implantation energy for the first and second steps were 140 keV and 50 keV, respectively. For device applications, such as HBTs, it is crucial to remove the damage and strain caused by the implantation [12, 13] usually by thermal annealing. The implanted SiC: Ge layers were annealed with our high- temperature annealing furnace and analyzed with High Resolution X-ray Diffraction (HRXRD), and Fourier Transform Infrared Spectroscopy (FTIR). This was a joint project with M. Dashiell and E. Ansorge, my role was to perform X-ray diffraction and FTIR measurements, and to analyze the data.

3.1 X-Ray Diffraction

The as- implanted SiC: Ge layer were investigated by high-resolution X-ray diffraction using a Philips X'Pert MRD diffractometer equipped with a four-crystal Ge (220) monochromator and a Ge channel-cut analyzer on the primary and detector optical arms, respectively. The X-ray wavelength was 1.54 Å and the diffractometer

acceleration voltage was 40 KV. The implanted samples with Ge concentrations ranging from 0.07 to 1.25 atomic percent were measured by XRD, I also measured 035% Ge doped SiC samples with different annealing temperatures(from 1250^0C to 1650^0C).

Fig. 3.1 shows the symmetric (0004) HRXRD spectra from the as-implanted SiC:Ge samples with Ge concentrations ranging from 0.07 to 1.25 atomic percent (implant doses are shown in the figure). The well resolved low-angle diffraction features at $\Delta\Theta=0$ are relative to the (0004) 4H-SiC substrate. Because the strained layer has a larger perpendicular lattice spacing than the bottom substrate, we observed broad higher-intensity diffraction peaks in a smaller diffraction angle relative to the main diffraction (0004) SiC peak. Pendellosung fringes were also observed due to the finite thickness of the strained layer. [14, 15] As can be seen from Fig. 3.1, the strain fringes built up during the ion implantation process increased with increasing implantation dose. The fringes disappeared at the highest doses, suggesting that the top implanted layer was relaxed to some degree at such a high dose.

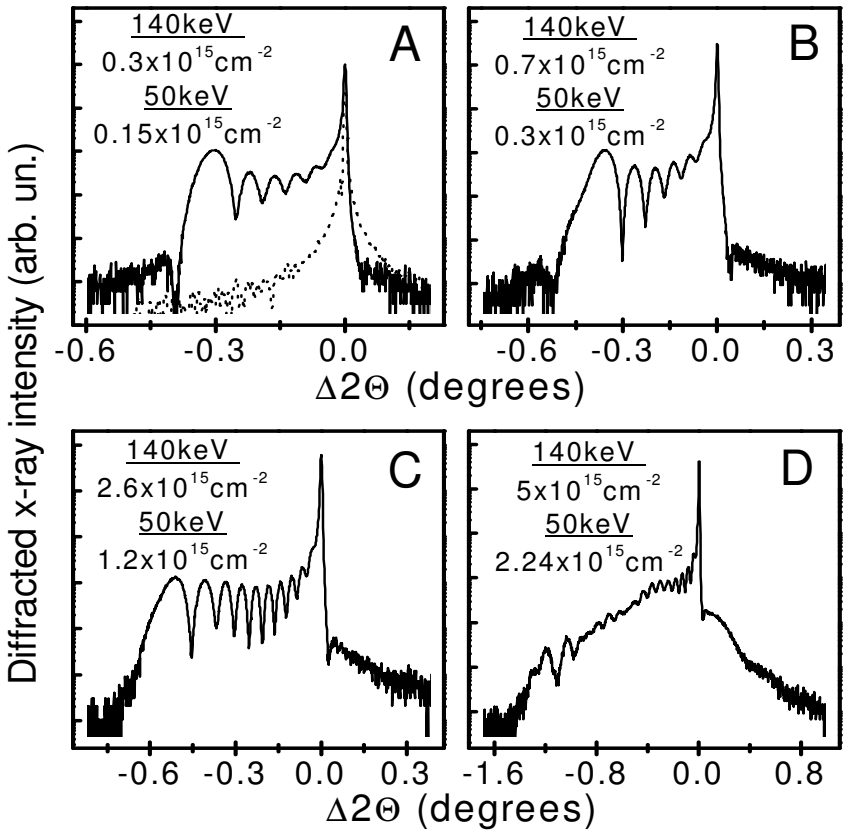

Figure 3.1: Experimental HRXRD spectra of implanted samples for Ge concentrations of (a) 0.074%, (b) 0.16%, (c) 0.6%, (d) 1.25%, with indicated energies and doses. The spectrum of the unimplanted 4H-SiC substrate is shown as the dotted line in (a). The horizontal axis have different scales to show the SiC:Ge layer peaks relative to the (0004) SiC substrate reflection.

0.35% Ge doped SiC samples were annealed in the temperature range from T_A=1250^{o}C to 1650^{o}C under Ar gas purge in a closed tube furnace for 10 minutes, not including the ramping up/down cycle of about 20 minutes. Fig. 3.2 shows the HRXRD spectra of the annealed samples, the X- Ray diffraction pattern of the as-implanted sample was also included for comparison. The spectra of the annealed samples differed dramatically from that of the as- implanted. All the annealed samples, however, showed similar X- Ray diffraction pattern, almost independent of annealing temperatures. This suggests that the strained SiC:Ge layer is metastable after implantation, but after annealing the compressive strain relaxed to a magnitude that is stable up to at least 1650^{o}C. The thickness fringes of the annealed samples indicate the layers remained pseudomorphic. This result differs from previously reported GaAs, Si and SiC where post-implant annealing *removed* the residual macroscopic strains observable with HRXRD. [16,17]

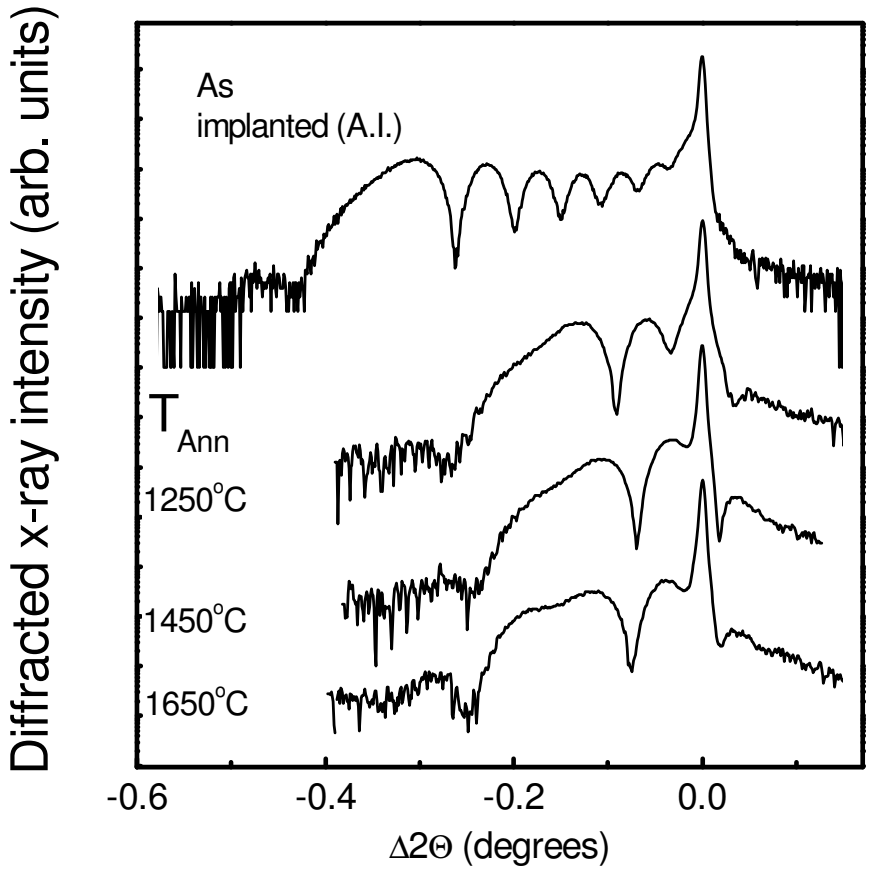

Figure 3.2: HRXRD (0004) reflection spectra of SiC:Ge samples (Ge=0.35%) as-implanted (A.I.), and after 10 minute furnace anneals at indicated temperatures.

3.2 Fourier Transform Infrared Spectroscopy (FTIR)

The as- implanted and annealed samples were analyzed with infrared reflectance measurements at room temperature in the spectral range from 500cm^{-1} to 2000cm^{-1}, using a Thermo Nicolet Nexus 870 Fourier Transform Infrared (FTIR) Spectrometer. A DTGS detector, KBr beam splitter, and variable angle specular reflectance accessory was used to perform the measurements. For the as- implanted samples, two interesting features were observed at 838 and 948 cm^{-1} as shown in Fig. 3.3. These two valleys were attributed to the axial folded transverse optic (FTO) mode, and the disorder mode respectively of 4H- SiC as the positions agrees well with previously published data. [18] These assignments were further confirmed with the polarization effects. As the reflection angle increased, the component of the incident electric field parallel to the c axis increased. Consequently, the valley in the reflectance spectra was deeper for higher reflection angel.

For the implanted samples, it is interesting to note that the valley at 948 cm-1 dissapeared at all the annealing temperatures as shown in Fig. 3.4. This suggests that annealing helps remove the strain and disorders caused by Ge ion implantation. Again, this results is in good agreement with the previous X- Ray measurement results.

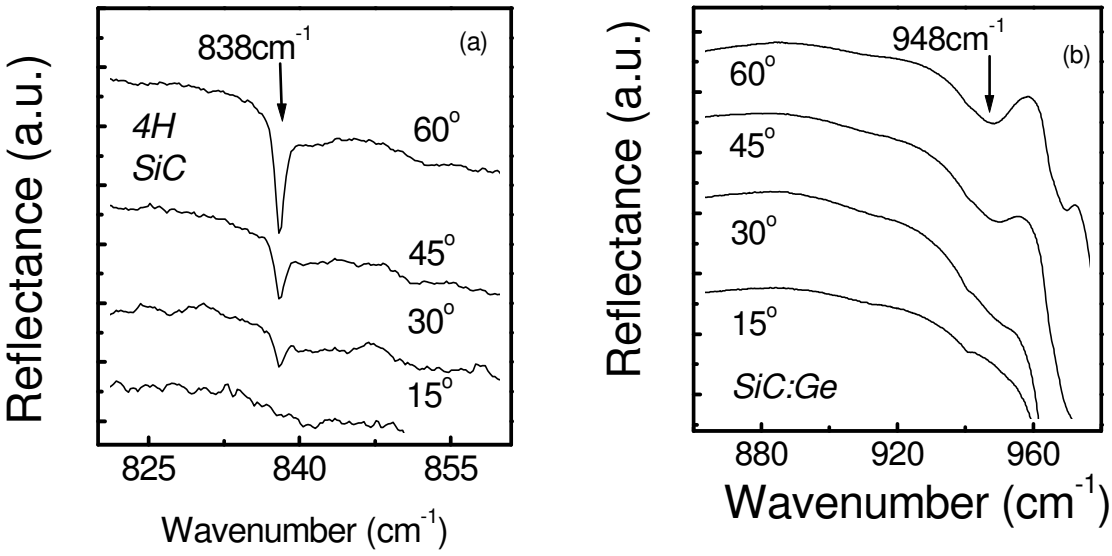

Figure 3.3: **(a) Dependence of IR reflectance (arbitrary units) on wavenumber and incident angle of the axial-folded-transverse-optical (FTO) phonon of the 4H-SiC substrate. (b) The angle dependence of the SiC:Ge (with Ge = 0.074%) related mode showing a similar angular dependence of mode intensity. The angle of incident light is taken with respect to the c-axis. The reflectance spectra in these figures have the same vertical scale factor, but are offset with respect to one another for clarity.**

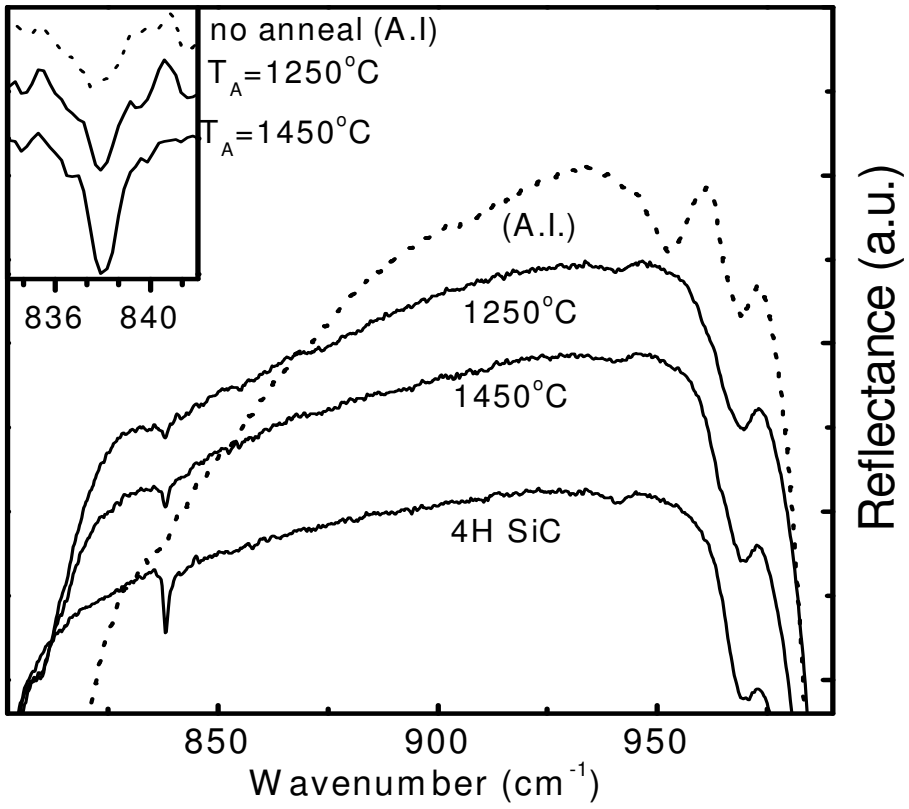

Figure 3.4: Infrared reflectance, where the incident light is an angle of 10^o with respect to the substrate plane, for the as-implanted sample (dotted line), and for the SiC:Ge layers annealed. The 4H-SiC substrate is shown again for reference. After annealing, the new 948cm^{-1} mode observed after implantation becomes broadened or reduced, and the 838 cm^{-1} 4H vibration reappears. The inset shows a close-up of the evolution of the 838cm^{-1} 4H-FTO mode with annealing.

In conclusion, the ion implantation of Ge into 4H-SiC at 1000^{o}C formed a strained pseudomorphic layer. Upon annealing, the strain partially relaxed to a magnitude that was stable to at least 1650^{o}C. X-ray diffraction and transmission electron microscopy revealed a pseudomorphic layer under all annealing conditions. The post-annealed SiC:Ge layer resumed the 4H-SiC stacking sequence with no evidence of precipitation or lattice damage other than a few stacking faults. These results indicated that thermally stable strained SiC heterostructures with high crystalline and interface quality can be formed via the implantation of Ge, suggesting the possibility of SiC based heterojunction and strain engineered devices by incorporating Ge.

Chapter 4

TERAHERTZ ELECTROLUMINESCENCE FROM NITROGEN DOPED 4H-SILICON CARBIDE

4.1 Introduction of terahertz emitters

Terahertz resides in the region from 0.3 to 10 THz. [19] Devices operating in this region has many identified applications, such as spectroscopy, [20] bioimaging and biosensing. [21,22] Because most chemicals have resonance in the terahertz region, terahertz can be used to differentiate different materials. Moreover, most of the packaging materials, such as plastic, wood and ceramic are transparent in the terahertz region. Terahertz can be used to scan objects hidden in a box. This is especially important for homeland security applications. We may expect in the near future, terahertz scanners may be used to replace X-Ray scanners in airport and customs to scan luggage. Due to all these reasons, there has been remarkable research activity on Terahertz (THz) emitters and lasers.[23-25] Many approaches have been used to realize terahertz emission, including photoconductive antenna, quantum cascade lasers, and optically pumped terahertz lasers. An ideal terahertz emitter would be electrically pumped and directly emit terahertz at temperatures higher or within the range achievable with thermoelectric coolers. Quantum cascade lasers (QCLs) have been reported at terahertz frequencies that operate above liquid nitrogen temperatures (up to

137 K in pulsed mode), with milliwatts of emitted power.[26] Such quantum well devices, however, require time consuming epitaxial fabrication. Alternative concepts based on shallow impurity intra- center transitions in bulk silicon [27- 30] have become attractive because they are much simpler and there is no need for quantum wells.

Impurity states in silicon have been well characterized, and doped silicon THz emitters use impact ionization to excite neutral impurities from their ground (freeze-out) states to produce radiative transitions. The non-equilibrium carriers that are excited to the conduction/ valence bands by impact can then relax to the bound upper levels through low energy acoustic phonon emission. [31, 32] For pairs of states with energy separation larger than the acoustic phonon step, the non-radiative relaxation was suppressed, and radiative transitions have resulted in THz emission and lasing. The detailed carrier excitation and capture processes are shown in Fig. 4.1.

In silicon, the operating temperature for such devices was limited by the small activation energies of impurities. At temperatures above 30K, few impurities remained in the ground state for impurity impact excitation, while the remaining impurities were thermally excited to the bands. For this reason, electroluminescence in doped silicon was observable only to slightly above 30K. [29] The choice of dopants with higher activation energy may increase the operating temperature by reducing the thermal excitation of the carriers to the band, but for deeper dopants in silicon the corresponding transition energy increases and falls above the THz region.

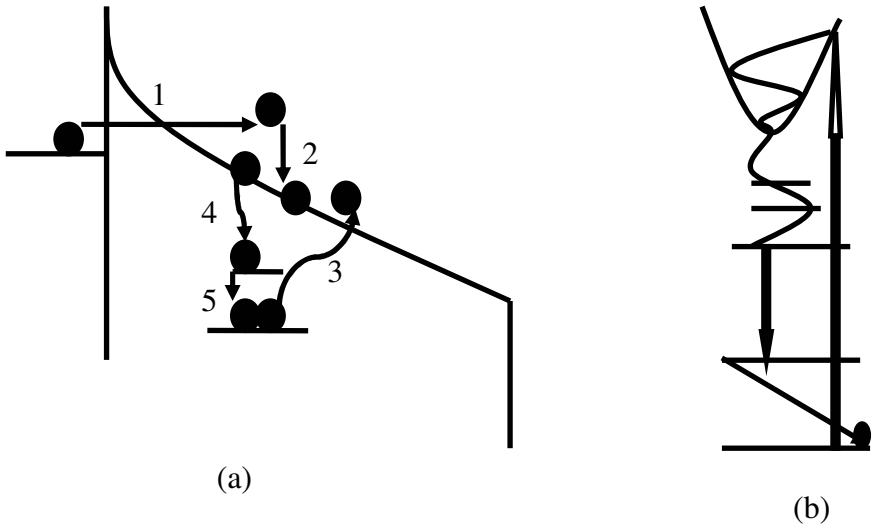

Figure 4.1: Current conduction and carrier excitation process in n-Si. (a) 1. electrons tunneling or leaking from the contact and acceleration in the space charge region, 2.Energy lost by impact ionization, 3. Excitation via impact ionization, 4. Cascade relaxation to excited state, 5. THz emission, (b) Excitation processes within an individual impurity center.

4.2 SiC Terahertz emitters

To increase the operating temperature of impurity doped terahertz emitters, we used the two inequivalent donor sites of nitrogen in 4H-SiC, one hexagonal and one cubic, with different energies as shown in Fig. 4.2. [33] Even up to room temperature, however, the impurities at the deeper cubic site are still only partially (~45%) ionized [34] and are available for impact excitation and transitions. The detailed energy levels and processes are depicted in Fig. 4.2 (b).At elevated temperatures, e. g. 77K, about 40% of the hexagonal donors are ionized to the conduction band, to supply electrons for impact ionization of the occupied donors. The purpose of this set of experiments was to study the possibility of using nitrogen doped SiC as high temperature terahertz emitters. This was a joint project with P.-C. Lv, my role was to fabricate the nitrogen doped 4H- SiC devices, and measure the electroluminescence with his help.

The devices were fabricated from 250 μm thick nitrogen-doped 4H- SiC wafers with room temperature resistivities of 0.11Ω-cm, corresponding to net doping concentration N_D-N_A= ~5E17cm^{-3} . The major compensation dopants determined by secondary ion mass spectrometry (SIMS) were boron (N_A ~1.16E17cm^{-3}) and Al (N_A~ 7.47E15 cm^{-3}). Photolithography was used to pattern photoresist into meshes with a filling factor of 50% for the topside electrical contacts, and the full wafer for the bottom contact. Metal contacts were formed by the e-beam evaporation of Ti/Au layers (20/500 nm) and photoresist liftoff. Devices were cleaved to a size of 2×2 mm^2, and

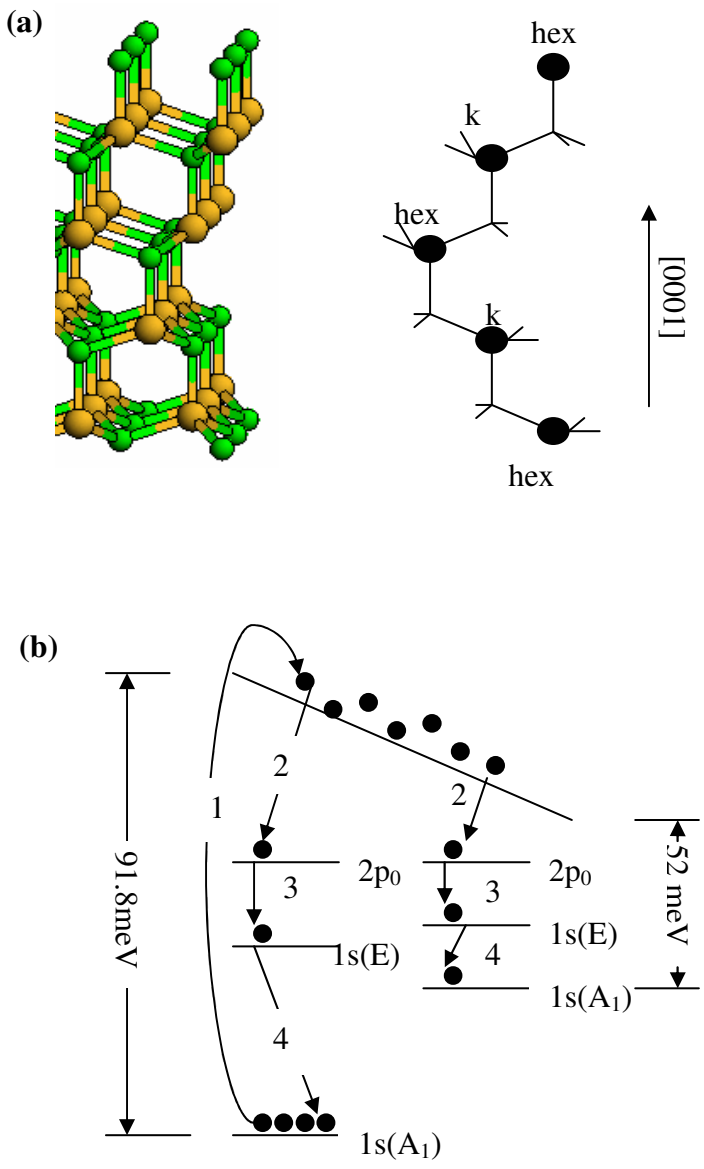

Figure 4.2: **(a) A schematic representation of the 4H-SiC crystal structure. The small and large disks represent C and Si atoms, respectively. There are two substitutional donor sites, cubic (k) and hexagonal (hex). (b) A schematic representation of the electron excitation and capture producing THz emission in 4H- SiC devices, showing the nitrogen donor cubic sites (left), and hexagonal sites (right).**

attached to a copper heat sink using silver epoxy. A micrograph of the fabricated devices is shown in Fig. 4.3.

After gold wire-bonding, the assembly was mounted in a liquid helium cryostat with a cesium iodide window. The coldhead temperature was measured by a platinum resistor. The emission from the top surface of the mesh structures was recorded with a Fourier Transform Infrared spectrometer (FTIR) (ThermoNicolet Nexus 870) with in the step-scan mode at a resolution of $4cm^{-1}$. A schematic of the measurement setup is shown in Fig. 4.4. Applying lateral current would be an alternative method to detect top emission. However, one needs to use insulating epoxy to isolate the devices from the copper heat sink to prevent vertical current conduction, which may have a shorter path. Because the insulating epoxy has a worse thermal conductivity compared to the silver epoxy, we used the vertical current conduction so that the temperature performance of our devices would not be underestimated. The detector was a liquid helium cooled silicon bolometer. Trains of 60 pulses with 375 ns:2.5 μs (width: period) at a repetition rate of 333 Hz were applied to the samples, and the current was measured by an inductive probe. The emitted power was calibrated by a blackbody radiator.

Fig. 4.5 shows a typical emission spectrum and five emission peaks were identified at wavenumbers of 261, 271, 298, 309 and 333 cm^{-1}. (corresponding to 7.83, 8.13, 8.94, 9.27 and 10 THz, respectively) The peaks at 309 and 333 cm^{-1} agreed well to previously reported absorption data (307 cm^{-1} and 333 cm^{-1}) corresponding to

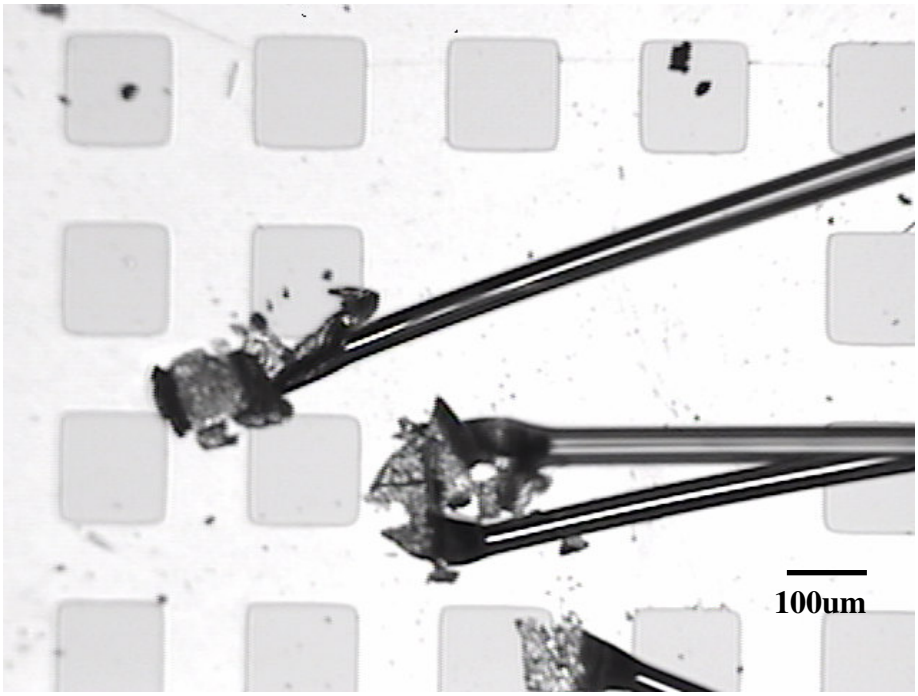

Figure 4.3: A top view of the fabricated and wired bonded SiC terahertz emitters. The emission was collected from the square openings from the top.

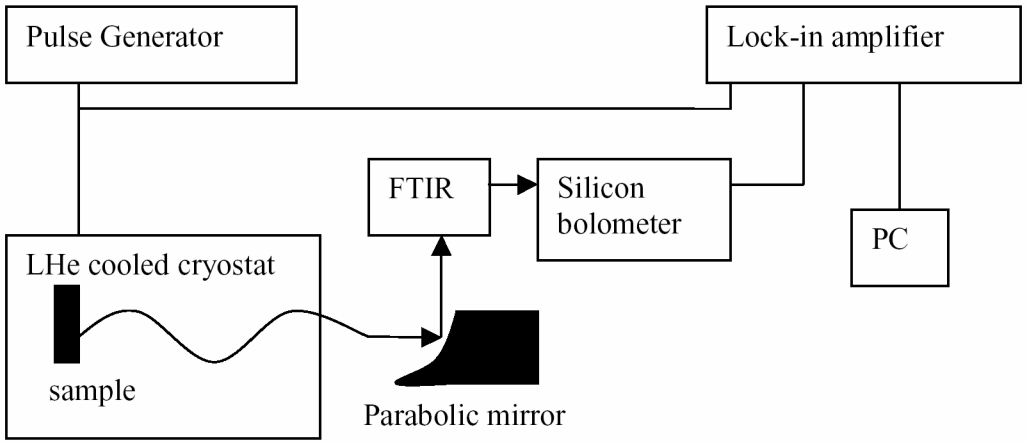

Figure 4.4: A block diagram of the experimental setup for THz electroluminescence measurements by Fourier transform spectroscopy.

the $2p_{+/-} \rightarrow 1s(E)$, and $3p_0 \rightarrow 1s(E)$ transitions, respectively, at the *hexagonal* donor site.

The separation between the emission lines at 261 and 298 cm^{-1} is the same as that between the $2p_{+/-}$(686 cm^{-1}) and $3p_0$ (724 cm^{-1}) *cubic* states reported by absorption measurements, within experimental error (1 cm^{-1}). Therefore, we attributed these two lines to the $2p_{+/-} \rightarrow 1s(E)$ and the $3p_0 \rightarrow 1s(E)$ states radiative transitions at the *cubic* donor site. Supporting evidence for these assignments comes from Raman measurements on different polytypes of SiC doped with nitrogen as performed by Colwell *et al.* [16] The $1s(A_1)$ to $1s(E)$ valley orbit transitions at the cubic sites were slightly dependent on polytype, and ranged from 46 meV in 15R-SiC to 62.6 meV in 6H-SiC. Because the valley-orbit splitting of the ground state of nitrogen donors at the cubic site cannot be determined by absorption (due to selection rules)[33], the energy position of the $1s(E)$ state at the cubic site was perviously unknown. In 4H- SiC, if the energy of the $1s(E)$ cubic state were 52.7 meV (425 cm^{-1}) above the $1s(A_1)$ state, then the transitions corresponding to $2p_{+/-} \rightarrow 1s(E)$ and $3p_0 \rightarrow 1s(E)$ would be at 261 and 299 cm^{-1}, remarkably close to the wavenumbers that we observed. The origin of the emission line at 271 cm^{-1} is not clear, but may be introduced by another dopant.

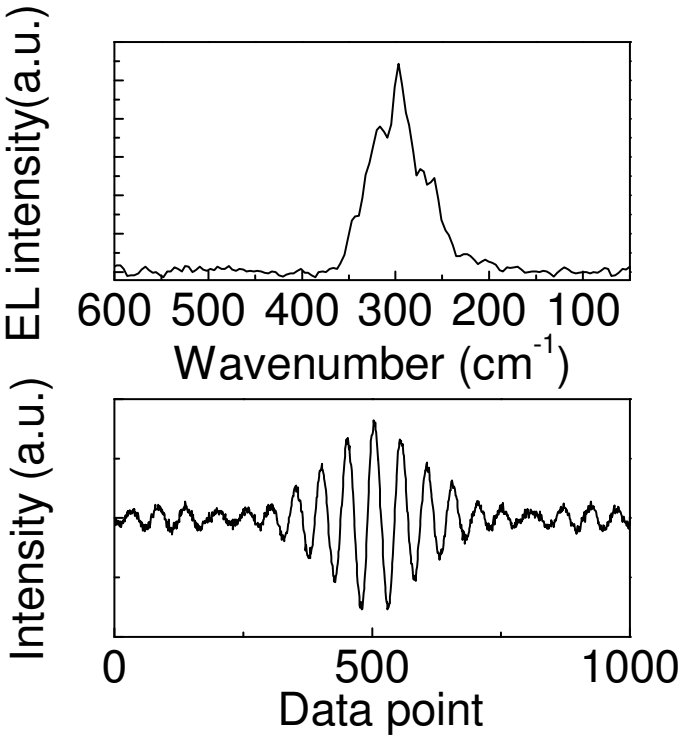

Figure 4.5: upper: Terahertz electroluminescence spectrum of nitrogen doped 4H-SiC emitters at 4K. lower: Interferogram collected in the step scan mode with 4cm^{-1} resolution, and 1000ms settling time and 1000ms collection time for each step.

As shown in Fig. 4.6, with increasing pumping current at 4K, the emission intensity increased but the shape of the spectra remained relatively the same, suggesting that the transition energies are field independent. Measurements above 77 K were performed with liquid nitrogen cooling. To reduce Joule heating, only 20 pulses per repetition train were used. The upper panel of Fig. 4.7 (a) shows that at 80 K, the emission spectrum broadened, but the features coincided with those at 4K, indicating that the emission was non-thermal. The intra- center transitions were associated with a regular pattern of the interferogram (lower panel of Fig. 4.7(a)) which differed qualitatively from that of blackbody radiation.

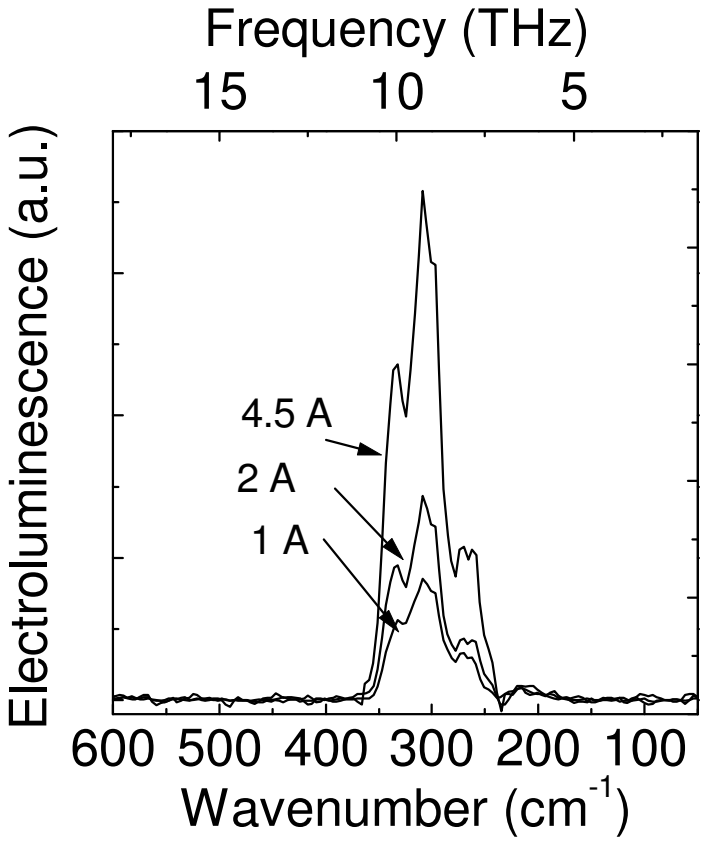

Figure 4.6: Evolution of the THz emission intensity with increasing pumping current at 4K.

Fig. 4.7(b) shows that as the temperature increased, the emission spectrum broadened, but peaks were still discernable up to 150K. Above 100K, we observed a change in the shape of the interferogram, associated with the appearance of blackbody radiation from resistive heating. This is because at higher temperatures fewer electrons were available in the donor states for radiative transitions even at the deeper cubic site.

The current-voltage (V-I) and light-output vs. current (L-I) curves of a typical device are shown in Fig. 4.8 At low temperature (4K), the sharp turn-on at 122 V was attributed to the electric field dependent impact ionization at the deeper cubic site. The shallower hexagonal donors were slightly depopulated by compensating acceptors, so that their ionization by the applied voltage was less abrupt, and a similar sharp turn- on of conduction at voltages lower than 122 V was not apparent. At higher temperatures (80K) the device behaved resistively with no clear turn-on, probably because of the current from thermally excited electrons. At higher voltages at both temperatures, the current saturated, which corresponded to the full ionization of the temperatures, the current saturated, which corresponded to the full ionization of the donors.

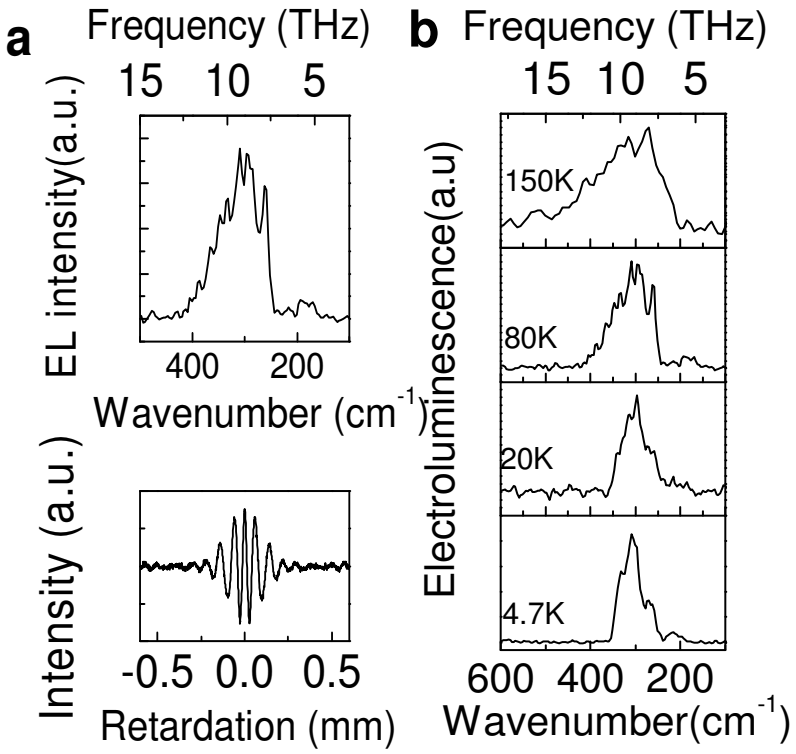

Figure 4.7: **(a) Top: THz emission spectrum of Nitrogen doped 4H- SiC devices with a pumping current of 2A at 80K. Bottom panel: regular pattern of the corresponding interferogram. (b) Evolution of the THz emission spectra with a pumping current of 2A.**

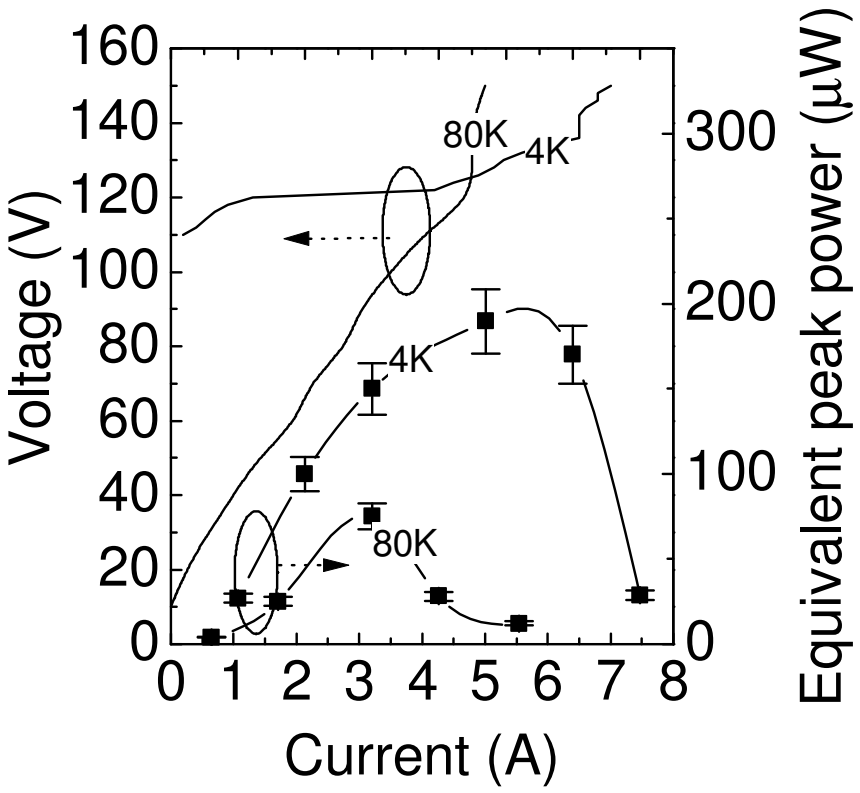

Figure 4.8: **Light output versus current L-I (red dashed lines) and V-I (black solid lines) characteristics of a typical device at 4K and 80K. The equivalent peak power is determined from the measured average power divided by the duty cycle of the electrical pulses.**

Accounting for the time-averaging duty cycle, the maximum peak emitted power, integrated from 1.5 THz to 18 THz, was ~190 μW with a current of 4.7A at 4K from the partially metalized top surface. This power measurement was calibrated by comparison with known emission from a recessed cone blackbody source. At each temperature, the total emitted power first increased with current, and then saturated and decreased. Because of the fixed ionized donor concentration, further increases of voltage would not affect the populations of electrons in the band. At high voltages, however, the electrons in the band would be more difficult to capture, resulting in less emitted power.

Our electrically driven nitrogen doped 4H- SiC THz emitting devices have the merits of simple design, fabrication, and high temperature operation (150K). The two ionization energies make possible the high power, high temperature operation of our THz devices. The working temperature of our devices is comparable to or exceeds the highest reported THz QCLs, [26] and is much higher than SiGe/ Si quantum cascade structures, and impurity based THz emitters, including the p-Ge [24] and doped silicon devices. [27-30] If a similar population inversion scheme can be built up in SiC as in optically pumped doped silicon lasers, [30] it may be an advantage to use SiC devices for high temperature and high power operation in the THz range of the electromagnetic spectrum.

Chapter 5

DISCUSSION AND CONCLUSIONS

In this thesis, a high temperature annealing furnace was designed, and assembled. Several engineering problems have been solved. The maximum temperature that the furnace can reach was 1450 ^{o}C, and the furnace has the capability of annealing samples at vacuum. I did all the design and construction myself with minimal assistance.

Ge ion implanted SiC samples were annealed, and characterized with high resolution X- Ray diffraction, and Fourier transform infrared spectroscopy. Our results suggest that high temperature annealing can remove the lattice damage and strain caused by ion implantation. In this joint project with M. Dashiell and E. Ansorge, I performed the X- Ray diffraction and FTIR measurements and analyzed the data. The results of these measurements were reported in a paper published on *Applied Physics Letter*. [11]

Using the two non- equivalent donor sites of nitrogen in 4H- SiC, terahertz emitters have been fabricated and characterized with electroluminescence measurements. For the first time, we demonstrated terahertz emission from SiC devices in the range from 7 to 12 terahertz. The maximum operating temperature was

150K, which was higher than many terahertz electroluminescence devices and comparable to the highest temperature of reported terahertz quantum cascade lasers. The peak emitted power was around 200 uW, which was higher than impurity doped silicon terahertz emitters, and SiGe/Si multiple quantum well structures. These results suggest that it may be an advantage to use SiC terhertz emitters for high temperature and high power portable applications. This was a joint project with P.-C. Lv, I fabricated the SiC terahertz devices and performed electroluminescence measurements with his help. I am the second author on a manuscript submitted to the journal of *Applied Physics Letter*.[35]

BIBLIOGRAPHY

1. A.A. Burk Jr., M.J. O'Loughlin, R.R. Siergiej, A.K. Agarwal, S. Sriram, R.C. Clarke, M.F. MacMillan, V. Balakrishna, and C.D. Brandt, *Solid-State Electronics*, **43**, 1459 (1999).

2. J.W. Palmour, S.T. Sheppard, R.P. Smith, S.T. Allen, W.L. Pribble, T.J. Smith, Z. Ring, J. Sumakeris, A.W. Saxler, and J.W. Milligan, *IEEE IEDM Technical Digest*, 385 (2001).

3. K.J. Roe , G. Katulka , J. Kolodzey , *Appl.Phys.Lett*. **78**, 2073 (2001).

4. G. Katulka , KJ. Roe , J. Kolodzey , *Appl. Surf. Sci* **175**, 505 (2001).

5. C. Guedj and J. Kolodzey, *Appl. Phys. Lett*., **74**, 691 (1999)

6. G. Katulka, C. edj, J. Kolodzey, R.G. Wilson, C. Swann, M.W. Tsao and J. Rabolt, *Appl. Phys. Lett*., **74**, 540, (1999).

7. M. Bhatnagar , BJ. Baliga , *IEEE Trans. Electron Devices* **40**,645(1993).

8. A. Bauer, J. Kräusslich, B. Köcher, K. Goetz, A. Fissel, W. Richter, *Mat. Sci. Eng*. **B61-61**, 179 (1999).

9. S. Nakashima , H. Matsunami , S. Yoshida , H. Harima , IOP publishing, Bristol, UK, 1 (1995).

10. MA. Capano , S. Ryu , MR. Melloch , Jr. Cooper , *J. Electron. Mater*. **27**,370(1998)

11. MW. Dashiell , G. Xuan , E. Ansorge , X. Zhang , J. Kolodzey , *Appl.Phys.Lett*. **85**,2253(2004).

12. T.T. Zorba, C.L. Mitsas, I.D. Siapkas, G.Z. Terzakis, D.I. Siapkas, Y. Pacaud, and W. Skorupa, *Appl. Surf. Sci*., **102**, 120 (1996).

13. Y. Paucaud, W. Skorupa, and J. Stoemenos, Nucl. Inst. and Meth. *Phys. Res. B*, **120**, 181 (1996).

14. Ch. Schubert, U. Kaiser, A. Hedler, and W. Wesch et al. *J. Appl. Phys*. **91**, 1520 (2002).

15. A. Declémy, E. Oliviero, M.F. Beaufort, J.F. Barbot, M.L. David, C. Blanchard, Y. Tessier, and E. Ntsoezok, . Inst. and Meth. *Phys. Res. B*, **186**, 318 (2002).

16. U. Zeimer, Semicond. *Sci. Technol*., 15, 965, (2000).

17. X. Duo, W. Liu, M. Zhang, X. Fu, J. Huang, C. Lin, *Nucl. Instr. and Meth. B* **170**, 98 (2000).

18. J.M. Bluet, K. Chourou, M. Anikin, and R. Madar, *Mat. Sci. Eng*. B61-62, 212 (1999).

19. R.A. Cheville, D.Grischkowsky, *Appl. Phys. Lett*., **67**, 1960,(1995)

20. F.C.Delucia, "Spectroscopy in the Terahertz Spectral region" in sensing with Terahert radiation .D. Mittleman, ed , Berlin, Springer- Verlay, 2003, pp, 39-115

21. PY. Han , GC. Cho ,XC. Zhang , *Opt Lett*, **25**, 242, (2000).

22. JL.Johnson , TD. Dorney , DW. Mittleman , *IEEE J, Select, Top. Quantum Elect*, **7(4)** 592,(2001).

23. R. Kohler , A. Tredicucci , F. Beltram , *nature*, **417**, 156,(2002).

24. MS. Kagan , IV.Altukhov , EG. Chirkova , VP. Sinis , RT. Troeger , SK. Ray , J. Kolodzey , *Phys, Stat, Sol,* (b), **235**, 135 (2003).

25. SG Pavlov , HW. Hubers , *J. Appl. Phys*., **9**2 5632,(2002).

26. S. Kumar, B. S. Williams, S. Kohen, Q. Hu, J. L. Reno, *Appl. Phys. Lett.* **84**, 2494 (2004); B. S. Williams, S. Kumar, H. Callebaut, Q. Hu, J. L. Reno, *ibid*, **83**, 5142 (2003).

27. T. N. Adam, R. T. Troeger, S. K. Ray, P. –C. Lv, and J. Kolodzey, *Appl. Phys. Lett.*, **83** 1713 (2003).

28. P.-C. Lv, R. T. Troeger, T. N. Adam, S. Kim, J. Kolodzey, I. N. Yassievich, M. A. Odnoblyudov, M. S. Kagan, *Appl. Phys. Lett.*, **85** 22 (2004).

29. P.-C. Lv, R. T. Troeger, S. Kim, S. K. Ray, K. W. Goossen, J. Kolodzey, I. N. Yassievich, M.A. Odnoblyudov, M. S. Kagan, *Appl. Phys. Lett.*, **85** 3660 (2004).

30. S. G. Pavlov, R. Kh Zhukavin, E. E. Orlova, V. N. Shastin, A. V. Kirsanov, H. –W. Hübers, K. Auen, H. Riemann, *Phys. Rev. Lett.* **84**, 5220 (2000).

31. V. N. Abakumov, I. V. Perel, I. N. Yassievich, " Nonradiative recombination in semiconductors" Modern Problems in Condensed Matter Sciences ed V. M. Agranovich and A. A. Maradudin (Amsterdam: North-Holland), 1991.

32. M. Lax, *Phys Rev.* **119**, 1502 (1960).

33. W. Gotz, A. Schoner, G. Pensl, W. Suttrop, W. J. Choyke, R. Stein, S. Leibenzeider, *J. Appl. Phys.* **73**, 3332 (1993).

34. M. A. Capano, J. A. Cooper, M. R. Melloch, A. Saxler, and W. C. Mitchel, *J. Appl. Phys.* **87**, 8773 (2000).

35. P.-C. Lv, X. Zhang, A. Powell, and J. Kolodzey, submitted to *Appl. Phys. Lett.* (2005).